Journal of
Materials Chemistry C

ROYAL SOCIETY
OF **CHEMISTRY**

PAPER

View Article Online
View Journal | View Issue

Check for updates

Cite this: *J. Mater. Chem. C*, 2020, 8, 5082

Magnetic transitions in exotic perovskites stabilized by chemical and physical pressure†

Yalin Ma,[a] Maxim S. Molokeev,[bcd] Chuanhui Zhu,[a] Shuang Zhao,[a] Yifeng Han,[a] Meixia Wu,[a] Sizhan Liu,[e] Trevor A. Tyson,[e] Mark Croft[f] and Man-Rong Li*[a]

Received 23rd December 2019,
Accepted 2nd March 2020

DOI: 10.1039/c9tc06976c

rsc.li/materials-c

Exotic perovskites significantly enrich materials for multiferroic and magnetoelectric applications. However, their design and synthesis is a challenge due to the mostly required recipe conditions at extremely high pressure. Herein, we presented the $Ca_{2-x}Mn_xMnTaO_6$ ($0 \leq x \leq 1.0$) solid solutions stabilized by chemical pressure assisted with intermediate physical pressure up to 7 GPa. The incorporation of Mn^{2+} into the A-site neither drives any cationic ordering nor modifies the orthorhombic *Pbnm* structure, namely written as $(Ca_{1-x/2}Mn_{x/2})(Mn_{1/2}Ta_{1/2})O_3$ with disordered A and B site cationic arrangements. The increment of x is accompanied by a ferromagnetic to antiferromagnetic transition around $x = 0.2$, which is attributed to the double-exchange interactions between A-site Mn^{2+} and B-site Mn^{3+}. Partial charge disproportionation of the B-site Mn^{3+} into Mn^{2+} and Mn^{4+} occurs for x above 0.8 samples as manifested by X-ray spectrum and magnetic behaviors. The coexistence of B-site Mn^{3+} (Jahn–Teller distortion ion) and B′-site Ta^{5+} (second-order Jahn–Teller distortion ion) could be energetically responsible for the absence of A-site columnar ordering as observed in other quadruple perovskites with half of the A-sites occupied by small transition-metal cations. These exceptional findings indicate that exotic perovskites can be successfully stabilized at chemical and intermediate physical pressure, and the presence of Jahn–Teller distortion cations at the same lattice should be avoided to enable cationic ordering.

Introduction

Perovskite oxides have attracted great interest because of their rich structural, magnetic, and electronic properties.[1–4] The stabilities and crystal systems of ABO_3 perovskites are represented by the octahedral factor $\mu = r_B/r_O$ and tolerance factor $t = (r_A + r_O)/\sqrt{2}(r_B + r_O)$ (r_O, r_A, and r_B stand for the ionic radii of the oxygen anion, the A- and B-site cations, respectively), proposed by Goldschmidt.[5,6] The radii of ions and tilting of octahedra have a significant impact on stabilizing perovskite structures in terms of their chemical, octahedral, stretch, and tilt limits.[7–12] In contrast to conventional perovskites that have large A-site cations, exotic perovskites can adaptively incorporate small cations (especially transition-metal ions) into the A-site.[13–16] A-site columnar-ordered quadruple perovskites, $A_2A'A''B_4O_{12}$, with 50% of small A-sites (denoted as square-planar coordinated A′ and tetrahedrally coordinated A″, respectively) were first discovered in the form of $Ca_2Fe'Fe''Ti_4O_{12}$ (also known as $CaFeTi_2O_6$ with A′ = A″ = Fe)[17] and then $Ca_2Mn'Mn''Ti_4O_{12}$ (known as $CaMnTi_2O_6$ with A′ = A″ = Mn).[18] $Ca_2Fe'Fe''Ti_4O_{12}$ crystallizes as a centrosymmetric *P*4$_2$/*nmc* (No. 137) structure, while $Ca_2Mn'Mn''Ti_4O_{12}$ adopts a polar *P*4$_2$*mc* (No. 105) structure in which Mn′ is off-set from the $Mn'O_4$ square-plane (Fig. 1a) rather than being exactly in the oxygen plane, as observed for Fe′ in the $Fe'O_4$ of $Ca_2Fe'Fe''Ti_4O_{12}$.[19] Rock-salt B-site ordering in $A_2A'A''B_2B_2'O_{12}$ (Fig. 1b) provides higher compositional freedom, as reported in the *P*4$_2$/*n* (No. 86) type $Ca_2Mn'Mn''B_2Re_2O_{12}$ (B = Mn,[20] Fe,[20] Co,[21] Ni[21]), $Ca_2Mn^{A'}Cu^{A''}(Fe_2)^{B}(Re_2)^{B'}O_{12}$,[20] and $R_2Mn'Mn''Mn_2Sb_2O_{12}$ (R = La, Pr, Nd, Sm).[22] The $A'O_4$ (square-planar), $A''O_4$ (tetrahedral), BO_6 (octahedral), and $B'O_6$ (octahedral) sites in $A_2A'A''B_2B_2'O_{12}$ are highly adaptable,[23] and can be occupied by the same element, as recently observed in RMn_3O_6 (R = Y, Gd, Dy, Ho, Er, Tm; A′ = A″ = B = B′ = Mn),[24–26] which crystallizes in the *Pmmn* (No. 59, Fig. 1c) space group and can be structurally written as $R_2^{3+}(Mn^{2+})^{A'}(Mn^{3+})^{A''}(Mn^{3+})_2^{B}(Mn^{3.5+})_2^{B'}O_{12}$, with layered charge ordering over the B-sites. When 75% of the A-sites are occupied by

---

[a] Key Laboratory of Bioinorganic and Synthetic Chemistry of Ministry of Education, School of Chemistry, Sun Yat-Sen University, Guangzhou 510275, China. E-mail: limanrong@mail.sysu.edu.cn
[b] Laboratory of Crystal Physics, Kirensky Institute of Physics, Federal Research Center KSC SB RAS, Krasnoyarsk 660036, Russia
[c] Siberian Federal University, Krasnoyarsk 660041, Russia
[d] Department of Physics, Far Eastern State Transport University, Khabarovsk 680021, Russia
[e] Department of Physics, New Jersey Institute of Technology, Newark, New Jersey 07102, USA
[f] Department of Physics & Astronomy, Rutgers, The State University of New Jersey, 136 Frelinghuysen Road, Piscataway, New Jersey 08854, USA

† Electronic supplementary information (ESI) available. CCDC 1972419–1972422. For ESI and crystallographic data in CIF or other electronic format see DOI: 10.1039/c9tc06976c

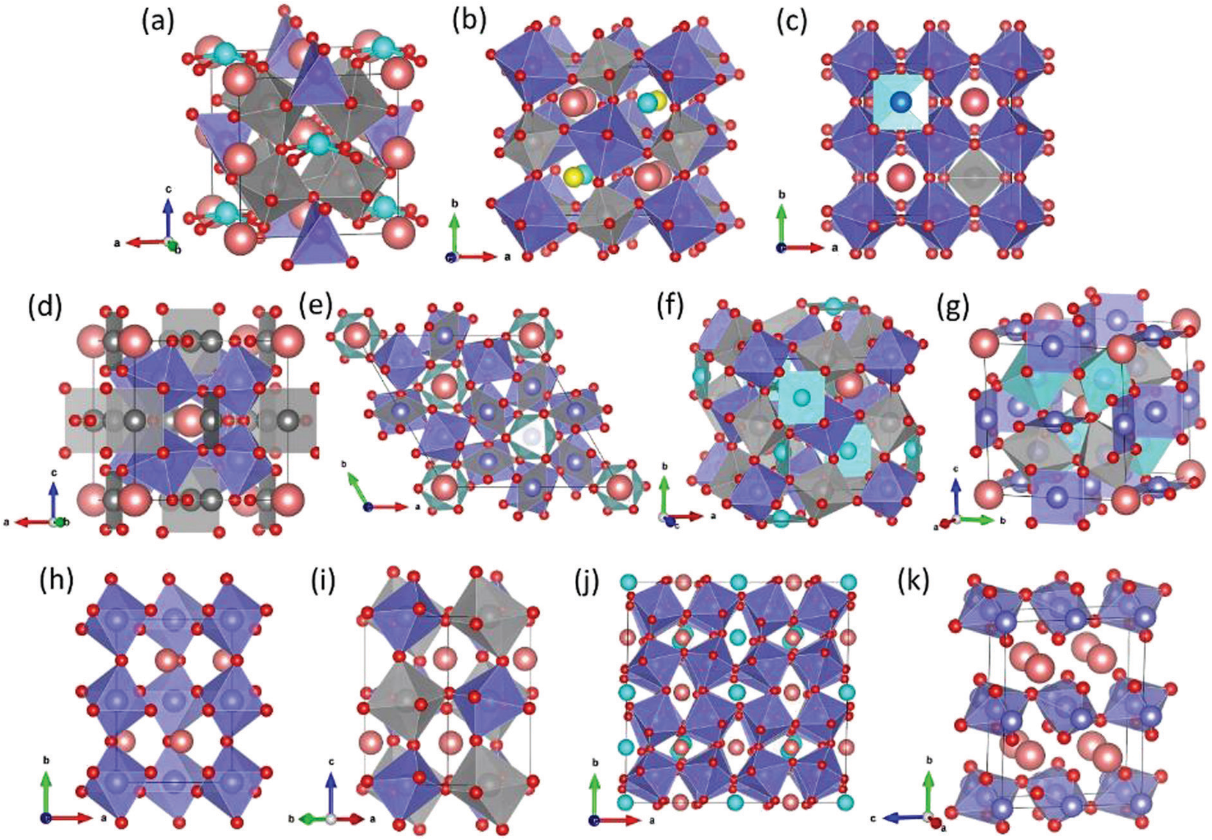

Fig. 1 Crystal structures of exotic perovskite oxides with small A-site cations. A, pink spheres; O, red spheres; BO_6 octahedra, violet; $B'O_6$ octahedra, silver gray; a_p represents the lattice parameters of a simple cubic perovskite. $A_2A'A''B_4O_{12}$ with 50% small cationic A-sites (A′ and A″): (a) A-site columnar-ordered quadruple perovskites $A_2A'A''B_4O_{12}$ (tetragonal, $P4_2mc$, $2a_p \times 2a_p \times 2a_p$ type). $A'O_4$ square-planar, cyan; $A''O_4$ tetrahedral, violet; BO_6 octahedra, silver gray. (b) Rock-salt B-sites ordering in $A_2A'A''B_2B_2'O_{12}$ (tetragonal, $P4_2/n$, $2a_p \times 2a_p \times 2a_p$ type). A′, cyan spheres; A″, yellow spheres. (c) RMn_3O_6 with layered charge ordering over the B-sites (orthorhombic, $Pmmn$, $2a_p \times 2a_p \times 2a_p$ type). $Mn1O_4$ square-planar, cyan; $Mn2O_4$ tetrahedral, silver gray; MnO_6 octahedra, violet. $AA_3'B_4O_{12}$ with 75% small cationic A-sites (A′): (d) most known $AA_3'B_4O_{12}$ quadruple perovskites (cubic, $Im\bar{3}$, $2a_p \times 2a_p \times 2a_p$ type). $A'O_4$ square-planar, silver gray. (e) B-site charge-ordering of $A^{2+}Mn_3Mn_4O_{12}$ (rhombohedral, $R\bar{3}$, as the subgroup of $a_p \times 2a_p \times 2a_p$ type $Im\bar{3}$). $Mn1O_4$ square-planar, silver gray; $Mn2O_6$ octahedra, violet; $Mn3O_6$ octahedra, cyan. (f) 1322-type B-site ordering of $AA_3'B_2B_2'O_{12}$ (cubic, $Pn\bar{3}$, $2a_p \times 2a_p \times 2a_p$ type). $A'O_4$ square-planar, cyan. (g) Trivalent A-site driving Jahn–Teller distorted Mn^{3+} component on the B-site of $A^{3+}Mn_7O_{12}$ (monoclinic, $I2/m$, $2a_p \times 2a_p \times 2a_p$ type), MnO_4 square-planar, violet; $Mn4O_6$ octahedra, silver gray; $Mn5O_6$ octahedra, cyan. Exotic perovskite with 100% small cationic A-sites: (h) $GdFeO_3$-based ABO_3-type (orthorhombic, $Pbnm$, $\sqrt{2}a_p \times \sqrt{2}a_p \times 2a_p$ type); (i) $A_2BB'O_6$-type (monoclinic, $P2_1/n$, $\sqrt{2}a_p \times \sqrt{2}a_p \times 2a_p$ type), (j) ζ-Mn_2O_3-type (triclinic, F-1, $4a_p \times 4a_p \times 4a_p$ type), and (k) post-perovskite (orthorhombic, $Cmcm$, $\sqrt{2}a_p/2 \times 2a_p \times \sqrt{3}a_p$ type).

small cations, $AA_3'B_4O_{12}$-type quadruple perovskites can be formed with square-planar coordinated A′-sites, such as A′ = Mn^{3+}, Co^{2+}, Cu^{2+}, Pd^{2+} in $LaMn_3V_4O_{12}$,[27] $LaCu_3Fe_4O_{12}$,[28] $CaCo_3V_4O_{12}$,[29,30] $CaPd_3Ti_4O_{12}$,[31,32] respectively. Most known $AA_3'B_4O_{12}$ quadruple perovskites are cubic $Im\bar{3}$ (No. 204) symmetry (Fig. 1d), unless B-site charge-ordering induced distortion occurs, as in rhombohedral manganite $A^{2+}Mn_3Mn_4O_{12}$ ($R\bar{3}$, No. 148, A = Ca, Cd, Pb, Pr, Sr, Fig. 1e).[33–35] 1322-type B-site ordering of quadruple perovskites, $AA_3'B_2B_2'O_{12}$, leads to symmetry evolution from $Im\bar{3}$ to $Pn\bar{3}$ (No. 201, Fig. 1f), such as reported in $CaCu_3Fe_2Re_2O_{12}$,[36] $CaCu_3Fe_2Nb_2O_{12}$,[37] and $NaCu_3Fe_2Os_2O_{12}$.[38] In the $A^{3+}Mn_7O_{12}$ (A = La, Pr, Nd) series, the trivalent A-site ion drives more Jahn–Teller distorted Mn^{3+} component on the B-site, which, together with charge ordering, results in a monoclinic $I2/m$ (No. 12) structure (Fig. 1g), as in $Pr^{3+}Mn_3{}^{3+}(Mn^{2.99+})_2{}^{B}(Mn^{3.01+})_2{}^{B'}O_{12}$.[39,40] The spatial effect of the $6s^2$-lone pair electrons of Bi^{3+} in $BiMn_7O_{12}$ further leads to the complex temperature-dependent symmetry evolution of $Im\bar{3}$ (above 608 K) – $I2/m$ (460–608 K) – Im (290–460 K) – $P1$ (below 290 K) upon cooling.[41] Full occupation of the A-site with small cations usually encourages pressure-dependent polymorph competition, and usually the perovskite phases need to be stabilized *via* higher pressure synthesis.[16,42–44] $GdFeO_3$-based $Pnma$ (No. 62, Fig. 1h) and $P2_1/n$ (No. 14) structures (Fig. 1i) have been successively discovered in ABO_3-type (such as $MnVO_3$ and $ScCrO_3$)[45–47] and $A_2BB'O_6$-type (such as Mn_2BSbO_6 (B = Fe,[43] Sc,[48] V[49]), Mn_2BReO_6 (B = Mn,[14,50] Fe,[15,51] Co[52]), and $Mn_2(Fe_{0.8}Mo_{0.2})MoO_6$)[13] perovskites, respectively. $AA_3'B_4O_{12}$-type quadruple perovskites can also be prepared in this category if the pressure is high enough, such as $ACu_3V_4O_{12}$ ($Im\bar{3}$, A = Cu, Mn), and ζ-Mn_2O_3 (structurally written as $Mn^{2+}(Mn^{3+})_3(Mn^{3.25+})_4O_{12}$, Fig. 1j, $P\bar{1}$ (No. 2)).[53–55] Post-perovskite structural compounds (Fig. 1k, $Cmcm$, No. 63) such as δ-Mn_2O_3 and $MgSiO_3$ can exist at extremely high pressure, but decompose during decompressing to ambient condition.[56,57]

Partial or full occupation of small cations at the A-sites in exotic perovskite not only leads to rich structural chemistry, but also provides a continuous impetus to search for new physical properties, as small A-site cations, especially transition-metal ions, enhance the quantum degrees of freedom such as the lattice, spin, charge, and orbitals. A reduced t can cause structural distortion, thus leading to large spontaneous electrical polarization (P_S) in noncentrosymmetric materials,[58,59] while transition-metal-rich lattices lead to robust magnetic interplay, thus creating a magnetoelectric effect.[15,28,51] For example, $CaMnTi_2O_6$ is the only lone-pair-electron free switchable ferroelectric double perovskite ($P_S \sim 24$ μC cm^{-2}),[18] demonstrating potential piezoelectric and ferroelectric-photovoltaic applications. $Ca_2Mn^{A'}Cu^{A''}(Fe_2)^{B}(Re_2)^{B'}O_{12}$ is an above room-temperature ferromagnet (Curie temperature, T_C, of 560 K) with large room-temperature magnetization and low-temperature switchable magnetoresistance.[20] $LaCu_3Fe_4O_{12}$ undergoes temperature-dependent charge transfer at around 400 K, accompanied by metal–insulator transition behaviour.[28] $CaCu_3Fe_2Re_2O_{12}$ is a ferrimagnetic ($T_C \sim 560$ K) half metal with a large saturated magnetization of 8.7 μ_B.[36] Mn_2FeReO_6 displays giant positive magnetoresistance up to 220%.[15,51] ζ-Mn_2O_3 is the hardest direct narrow bandgap semiconductor, showing switchable p–n electronical conduction and spin-induced multiferroicity.[53–55] This list of examples could be even longer. However, these exotic perovskites are thermodynamically metastable and need to be prepared at high-pressure (usually above 6 GPa) and temperature (HPT). This costly procedure and small-scale sample amount (usually on the milligram level) significantly limit the applications of these materials. Therefore, synthesis under ambient or much lower pressure, which remains a challenge, is highly desired.

Recently, Zhou *et al.* successfully stabilized a gram-scale high-pressure $Ca_{2-x}Mn_xTi_2O_6$ ($x \leq 0.6$) phase under a very modest pressure (below 0.1 GPa).[19] $Ca_{1.4}Mn_{0.6}Ti_2O_6$ is isostructural with $CaMnTi_2O_6$ ($P4_2mc$) and shows similarly high ferroelectric transition temperature. These findings suggest that it is possible to achieve large-scale high-pressure product driven by chemical potential (pressure)[60] and very modest physical pressure. Understandably, Ca^{2+} and Mn^{2+} have the same charge and slightly different ionic radii (at eight coordination, ${}^{VIII}r(Ca^{2+}) = 1.12$ Å, ${}^{VIII}r(Mn^{2+}) = 0.96$ Å),[61] so that the chemical pressure can assist to underpin Mn^{2+} into the Ca^{2+} matrix. In this work, we report a perovskite solid solution of $Ca_{2-x}Mn_xMnTaO_6$ ($0 \leq x \leq 1.0$) stabilized by the combination of chemical and physical pressure, and the intensive study of the composition-dependent evolution of the crystal structure, formal oxidation states of the cations, and its magnetic properties.

Experimental

Synthesis

The Ca_2MnTaO_6 (CMTO) precursor was prepared *via* solid-state reactions with appropriate stoichiometric amounts of $CaCO_3$ (MACKLIN, 99.99%), Mn_2O_3 (Sigma-Aldrich, 99.99%), and Ta_2O_5 (Alfa Aesar, 99.993%). The mixture was ground and pressed into pellets, and calcined at 1275 K for 8 h to decompose the carbonate. Then, the product was reground and pressed into pellets, and sintered in air for two periods of 48 h at 1653 K with intermediate grinding and pelletizing. $Ca_{2-x}Mn_xMnTaO_6$ samples with $x = 0.2$, 0.4, 0.6, 0.8, 1.0, 1.5, 1.6 and 2.0 were synthesized from the stoichiometric mixtures of the as-prepared CMTO, MnO (Alfa Aesar, 99.99%), Mn_2O_3, and Ta_2O_5. Samples with $x = 0.2$ were heated at 1625 K for 24 h under ambient pressure (AP), whereas $x = 0.4$–2.0 were prepared in a Walker-type multi-anvil apparatus at 1523–1625 K under 5–8 GPa for 30 min in Pt capsules and then quenched to room temperature, followed by a gradual release of the pressure. Around 0.5 g and 80 mg of sample can be prepared for each run below and above 5 GPa, respectively, in our syntheses.

Powder X-ray diffraction and energy dispersive X-ray spectroscopy

Powder X-ray diffraction (PXRD) data were collected at room temperature on a RIGAKU RINT-2000 diffractometer using Cu-Kα radiation ($\lambda = 1.5418$ Å). Here, the 2θ range between 10° and 120° with a step size of 0.02° was measured, using a counting time of 3.93 s per step at 40 kV and 26 mA. The TOPAS 4.2 software package[62] was applied to perform diffraction data analysis and Rietveld refinement. Cross-sectional scanning electron microscopy (SEM) with energy-dispersive X-ray spectroscopy (EDS) images were recorded using a FEI Quanta 400F with an Oxford-instruments INCA 400 EDS detector operating at an accelerating voltage of 20 kV. The EDS elemental composition was expressed quantitatively as weight percentage or atomic percentage.

X-ray absorption near edge and photoelectron spectroscopy

Mn-K and Ta-$L_{2,3}$ X-ray absorption near edge spectroscopy (XANES) data were collected in both fluorescence and transmission modes with simultaneous standards. All of the spectra were fitted to linear pre- and post-edge backgrounds and normalized to the unity absorption step across the edge.[13,63,64] $Ca_{1.8}Mn_{0.2}MnTaO_6$ XANES measurements were performed at the Brookhaven NSLS-II on the QAS 7-BM beamline using a Si-111 channel cut monochromator. Most of the standard spectra were recorded on X-19A at NSLS-I with a Si-111 double crystal monochromator. X-ray photoelectron spectroscopy (XPS) measurements were performed on a Nexsa XPS system equipped with a monochromatic Al Kα X-ray source ($h\nu = 1486.6$ eV) operated at 720 W, and the background pressure was kept at around 2×10^{-9} mbar. All binding energies were calibrated using surface contaminant carbon (C 1s = 284.8 eV) as a standard to scale.

Magnetic measurements

Magnetic measurements were implemented using a physical properties measurement system (PPMS, Quantum Design). The temperature-dependent magnetization was measured in zero field cooled (ZFC) and field cooled (FC) modes over a temperature range of 5–400 K under a 0.1 T magnetic field (H). The field dependence of isothermal magnetization was measured under an applied magnetic field varying from −5 to 5 T between 5 and 300 K.

Results and discussion

Synthesis and structural characterization

The degree of cationic ordering and octahedral tilting in double perovskite oxides is kinetically dependent on synthetic conditions, as in Ca_2MnTaO_6, which was reported to be monoclinic $P2_1/m$ (No. 11, ordered Mn and Ta at the B-sites)[65] or competitive orthorhombic *Pbnm* (disordering arrangement of Mn and Ta),[66] reported by different researchers. In our case, all of the $Ca_{2--x}Mn_xMnTaO_6$ ($0 \leq x \leq 2.0$) samples synthesized under AP and HP are black in colour. Both the $x = 0$ and 0.2 phases can be stabilized by chemical pressure only and synthesized under AP, with a better orthorhombic *Pbnm* structure, as observed from the PXRD patterns (Fig. 2a). Chemical pressure alone is not enough to stabilize the $x = 0.4$ and 0.6 samples, since impurity peaks are observed alongside the target phase, as shown in Fig. S1a and c (ESI†). Attempts to purify the $x = 0.4$ and 0.6 series with additional physical pressures between 2 and 5 GPa were unsuccessful, since the impurity phases can be suppressed at higher pressure but are still distinct in the PXRD patterns of the 5 GPa products (Fig. S1b and d, ESI†). Therefore, higher physical pressure is required to stabilize and drive the formation of a pure phase with x above 0.4. Fig. 2a clearly shows that a pure orthorhombic phase can be obtained for $0.4 \leq x \leq 1.0$ at 7 GPa. The chemical compositions of selected ($x = 0.4$–1.0) samples were confirmed from EDS analyses (Table S1, ESI†). No single phase was achieved for x above 1.5 up to 8 GPa, as shown in Fig. S1e–i (ESI†), where MnO and $Mn_3Ta_2O_8$ related phases were observed to be dominant in the $x = 2.0$ (Mn_2MnTaO_6) trial (Fig. S1h and i, ESI†). Conclusively, chemical pressure can adequately underpin Mn^{2+} at the Ca^{2+} site in $Ca_{2-x}Mn_xMnTaO_6$ for an x value of around 0.2, and additional physical pressure of 7 GPa can assist in pumping the phase boundary (x) at around 1.0 ($CaMnMnTaO_6$) but less than 1.5 ($Ca_{0.5}Mn_{1.5}MnTaO_6$). A single phase in different structure type(s) may exist at higher pressure for $x > 1.0$ in $Ca_{2-x}Mn_xMnTaO_6$, which is, however, not the theme of this work.

The PXRD peak evolution of $Ca_{2-x}Mn_xMnTaO_6$ is highlighted in the magnified 2θ areas between 21°–25° and 31°–34°, shown in Fig. 2b. The peaks continuously shift toward a higher degree (right) with increasing x, suggesting the successful incorporation of Mn^{2+} into the Ca^{2+} sites, regardless of the difference in their ionic radii. The main peak between 32°–33° is somewhat broadened in the $x = 0.6$ case compared with the others, suggesting degradation of the symmetry or the coexistence of two phases with very similar unit cell parameters. Structure refinements were conducted for all $x = 0$–1.0 samples, as shown in Fig. 3, and the corresponding crystal structures are presented in Fig. 4. The crystal structures, apart from $x = 0.6$, can be well refined as orthorhombic cells (*Pbnm*), starting from a model of La_2MgTiO_6.[67] The supercell of $Ca_{2-x}Mn_xMnTaO_6$ is around $\sqrt{2}a_p \times \sqrt{2}a_p \times 2a_p$, where a_p represents the lattice parameters of a simple cubic perovskite ($\sim$ 3.86 Å). The PXRD patterns of the $x = 0.6$ sample can be well fitted by two *Pbnm* phases with similar cell parameters, which appear to be x values of around 0.51(1) ($Ca_{1.49(1)}Mn_{0.51(1)}MnTaO_6$, 57(5)% by weight) and 0.32(1) ($Ca_{1.68(1)}Mn_{0.32(1)}MnTaO_6$, 43(7)% by weight) phases if extrapolated from the x-dependent orthorhombic lattice parameter a, b, and c evolution diagram shown in Fig. 5a. In the initial structural model, the La and Mg/Ti ions in La_2MgTiO_6 were replaced by Ca/Mn and Mn/Ta ions, respectively, with fixed occupancies according to the suggested chemical formula. The refined structural parameters and the coordinates of the atoms are shown in Table S2 (ESI†), and selected bond lengths and (Mn1/Ta1)O_6 octahedral distortion parameters are listed in Table S3 (ESI†). Although the PXRD data analyses show cationic disordering at both the A- and B-sites, there must be short-range local ordering driven by the atomic potential fields, resulting in size and/or charge difference between Ca/Mn and Mn/Ta. This very local short-range ordering is highly disordered and distributed at random, and is not enough to break the overall *Pbnm* symmetry, but results in relatively high atomic displacement parameters for the cations (Table S2, ESI†). Otherwise, superstructure peaks of the monoclinic structure would appear. Cationic ordering may

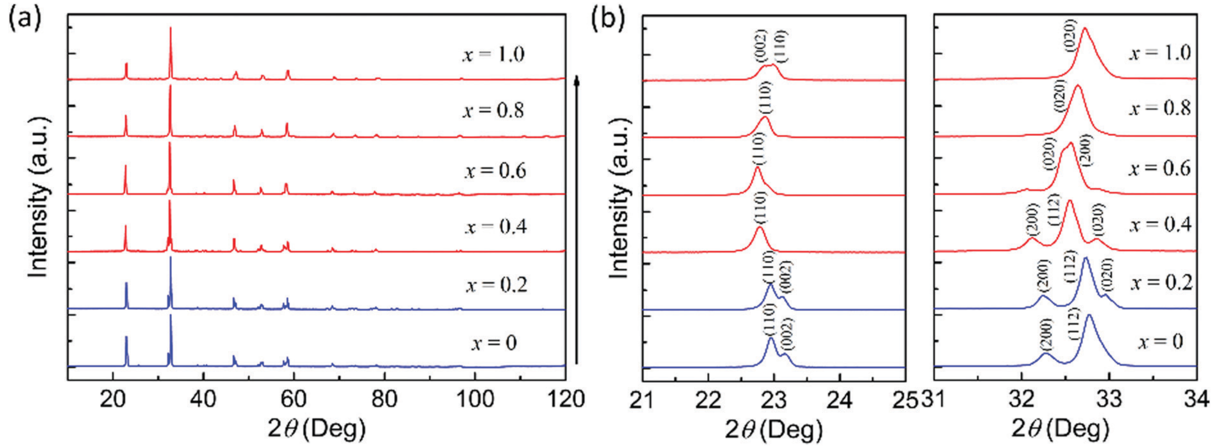

Fig. 2 (a) PXRD patterns of $Ca_{2-x}Mn_xMnTaO_6$ with x = 0, 0.2, 0.4, 0.6, 0.8 and 1.0, where the blue and red lines denote the phase prepared at AP and HP, respectively. (b) The magnified PXRD patterns between 21°–25° (left) and 31°–34° (right).

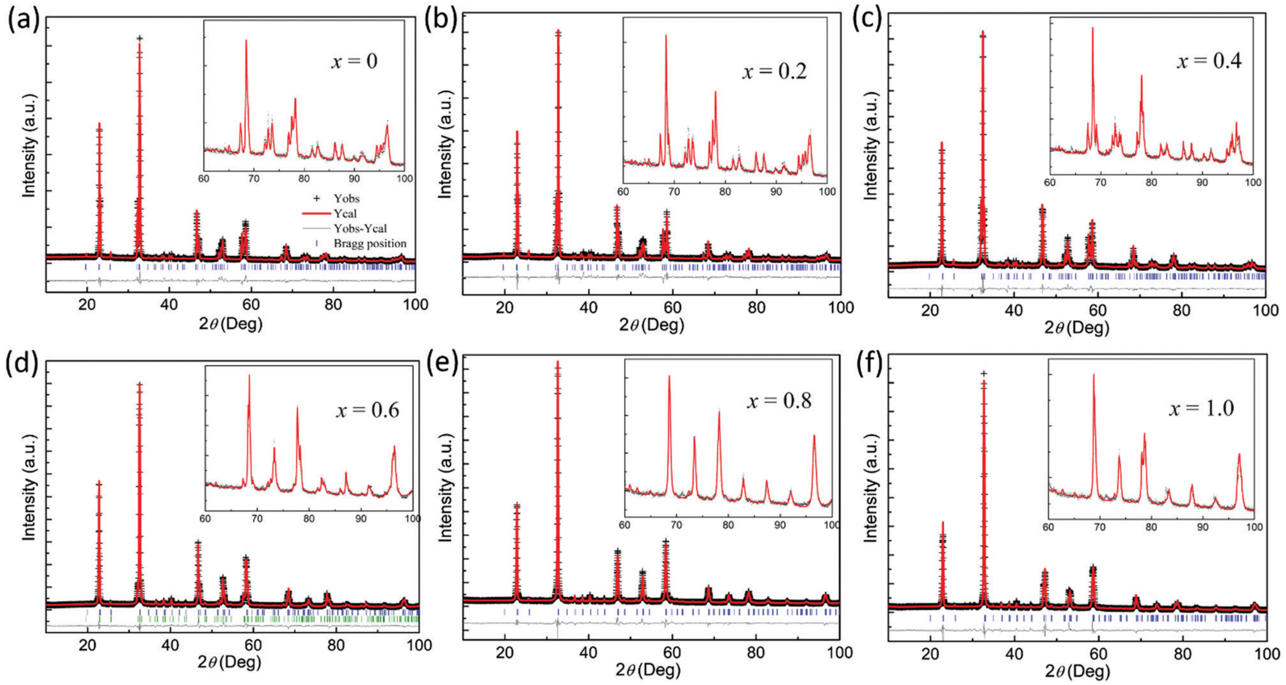

Fig. 3 Rietveld refinement of the PXRD patterns of $Ca_{2-x}Mn_xMnTaO_6$: (a) $x = 0$; (b) $x = 0.2$; (c) $x = 0.4$; (d) $x = 0.6$; (e) $x = 0.8$; (f) $x = 1.0$. The insets (60°–100°) show the magnified views.

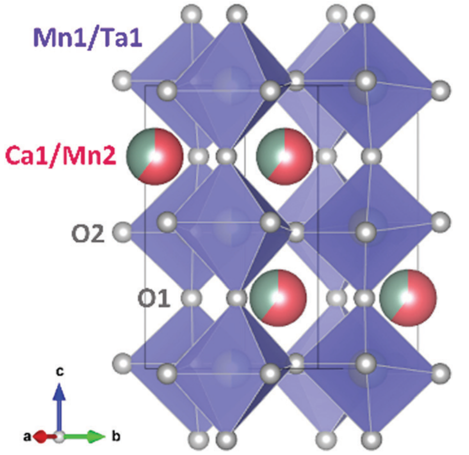

Fig. 4 Crystal structure of $Ca_{2-x}Mn_xMnTaO_6$. Ca1/Mn2 are located at the A site and Mn1/Ta1 are disordered over the B site. The violet octahedra are $(Mn1,Ta)O_6$.

arise in the high-pressure synthesized $Ca_{2-x}Mn_xMnTaO_6$ if it is cooled down slowly in the synthesis procedure, as reported for $CaCu_3Fe_2Nb_2O_{12}$.[37] The evolution of the unit cell dimensions loosely follows Vegard's law (Fig. 5a),[68] and the deviation may be attributed to the effect of physical pressure. The average bond lengths of (Ca1/Mn2)–O1, (Ca1/Mn2)–O2, (Ta1/Mn1)–O1, and (Ta1/Mn1)–O2 show small fluctuations (Fig. 5b). The bond valence sum (BVS) calculations suggest that the A-site (Ca1/Mn2) is under bonded with increasing *x*, while the B-site (Mn1/Ta1) is over bonded. To further confirm the formal oxidation state of the cations in $Ca_{2-x}Mn_xMnTaO_6$, XANES and XPS measurements were conducted for selected samples.

XANES and XPS analyses

The Mn-K main edge of $Ca_{1.8}Mn_{0.2}MnTaO_6$ is shown in Fig. 6a along with a series of standard spectra for comparison.[69–71] The $Sr_2Mn^{2+}ReO_6$, and $Ca_2Mn^{3+}TaO_6$ and $CaMn^{4+}O_3$ spectra illustrate a systematic "chemical shift" of the Mn-K edge, for Mn on the perovskite B-site, to higher energy with increasing formal Mn-valence.[69–71] The $Mn_2{}^{2+}FeReO_6$ spectrum, on the other hand, shows a much lower energy onset and peak typical for Mn^{2+} at the perovskite A-site.[63,72] Close inspection of the $Ca_{1.8}Mn_{0.2}MnTaO_6$ spectrum indicates that there is a dominant perovskite-B-Mn^{3+} component based on the proximity of the main peak to that of $Ca_2Mn^{3+}TaO_6$, and a much smaller perovskite-A-Mn^{2+} component based on the excess spectral weight below the peak in the energy range where the $Mn_2{}^{2+}FeReO_6$ spectrum peaks lie. To emphasize this difference, spectrum (Diff. Spect. in the Fig. 6a-top) was calculated by first subtracting the appropriately weighted $Ca_2Mn^{3+}TaO_6$ spectrum from the $Ca_{1.8}Mn_{0.2}MnTaO_6$ spectrum and the results were normalized to the standard unity absorption across the edge. Despite the crudeness of this approximation, the difference spectrum manifests a very clear spectral peak at precisely the peak energy of the perovskite-A-site standard $Mn_2{}^{2+}FeReO_6$. Thus, there is a strong conclusion that the Mn-K edge results support the ~Mn^{3+} (perovskite-B-site) and ~Mn^{2+} (perovskite-A-site) assignments, respectively, for the Mn and $Mn_{0.2}$ components in the $Ca_{1.8}Mn_{0.2}MnTaO_6$ compound formula.

The prominent bimodal A/B peak features in the 5d-row $L_{2,3}$ edge features, in octahedrally coordinated oxides, have been useful probes of d-configuration/valence by virtue of the systematic decrease in the A (t_{2g}-hole related) feature intensity, relative to that of the B (e_g-hole related) feature. The systematic A-feature spectral weight decrease with increasing d-count (decreasing t_{2g}-hole

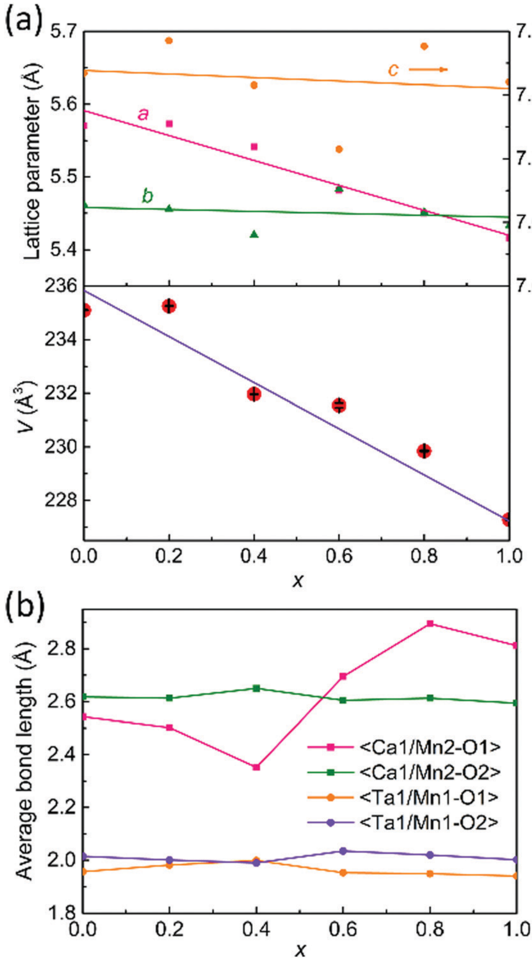

Fig. 5 Mn^{2+} ion concentration dependence of (a) the orthorhombic lattice parameter *a* (Å), *b* (Å), *c* (Å), the unit cell volume *V* (Å^3), and (b) average bond lengths in $Ca_{2-x}Mn_xMnTaO_6$ refined from PXRD data.

count) is clearly illustrated in Fig. 6b and c for standard 5d-row compounds between d^0 and d^5.[69,70,73,74] The Ta-$L_{2,3}$ edge spectra of $Ca_{1.8}Mn_{0.2}MnTaO_6$ is plotted as a solid red line in Fig. 6b and c and its large A-feature intensity very clearly supports the d^0/Ta^{5+} configuration/valence assignment for this compound. In summary, the XANES results for $Ca_{1.8}Mn_{0.2}MnTaO_6$ manifest an A-site $\sim Mn^{2+}$, a B-site $\sim Mn^{3+}$, and a B′-site d^0/Ta^{5+} states.

As shown in Fig. S2 (ESI†), the XPS spectrum for the Mn $2p_{3/2}$ region of $CaMnMnTaO_6$ ($x = 1.0$) was recorded and fitted using XPS standard software. The spectrum exhibits three main peaks at around 640.6, 641.8, and 644.0 eV, respectively. The binding energy values are in good agreement with Mn^{2+}, Mn^{3+}, and Mn^{4+} oxidation states, as reported in the literature.[75,76] It should be pointed out that Mn^{2+} is attributed to A-site Mn ions and Mn^{3+} corresponds to B-site Mn ions. The appearance of Mn^{4+} is derived from the charge disproportionation of Mn^{3+} into Mn^{2+} and Mn^{4+} at B-sites.[77,78] Based on the calculated percentage XPS peak areas, the amounts of Mn^{2+}, Mn^{3+} and Mn^{4+} are summarized in Table S4 (ESI†), which suggests the appearance of 10% of Mn^{4+} and Mn^{2+}, respectively, from the divergence of 20% of Mn^{3+}.

Magnetic characterization

Fig. 7 shows the temperature-dependent zero-field-cooled (ZFC) and field-cooled (FC) magnetic susceptibilities (χ) for x = 0–1.0 samples measured at 0.1 T. The paramagnetic susceptibility data were fitted to the Curie–Weiss (CW) law $\chi = C/(T - \theta)$ at temperatures above 150 K, where $C = \mu_{\text{eff}}^2/8$ is the Curie constant, θ is the Weiss temperature, and μ_{eff} is the effective magnetic moment. In Fig. 7a, the resulting θ = 39.4 K for x = 0 indicates that the predominant magnetic interactions are ferromagnetic (FM) transition. The divergence between FC and ZFC data in the magnetic susceptibility at T_1 = 19.6 K suggests that this is the FM transition temperature. It also implies that magnetic transition is due to spin-only Mn^{3+} (S = 2) and $Mn^{3+}–O^{2-}–Mn^{3+}$ super-exchange interactions, corresponding to $\mu_{\text{eff}} = 5.33\ \mu_B$ f.u.$^{-1}$ It needs to be mentioned that an anomaly

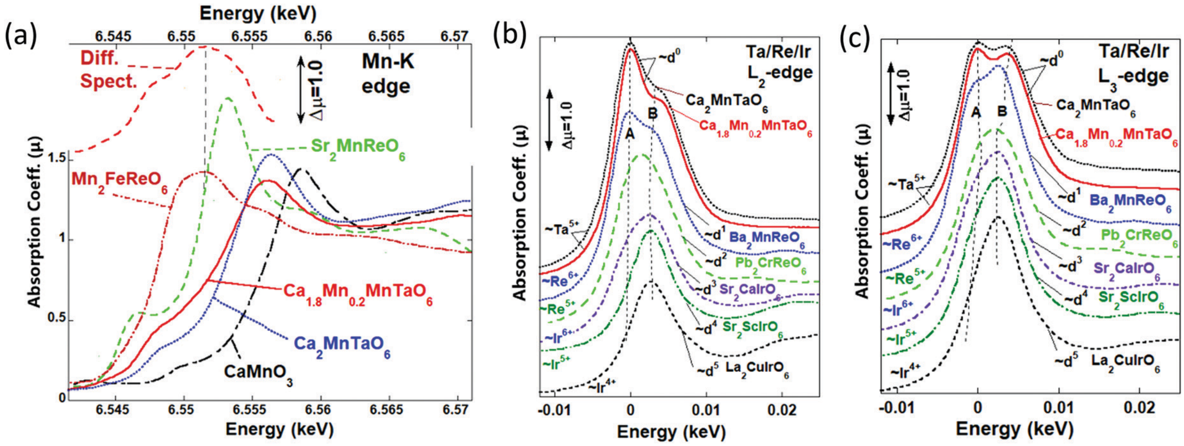

Fig. 6 (a) The Mn-K edge spectra for $Ca_{1.8}Mn_{0.2}MnTaO_6$, compared with those of a series of standard compound spectra: the A-site perovskite based $Mn_2^{2+}FeReO_6$; the B-site perovskite based $Sr_2Mn^{2+}ReO_6$, $Ca_2Mn^{3+}TaO_6$ and $CaMn^{4+}O_3$. The spectrum labeled as "Diff. Spect." is a weighted difference spectrum (with normalization) to estimate the A site Mn spectrum in $Ca_{1.8}Mn_{0.2}MnTaO_6$. (b) A superimposed comparison of the Ta-L_2 and L_3 edge of $Ca_{1.8}Mn_{0.2}MnTaO_6$ to those of the d^0/Ta^{5+}-Ca_2MnTaO_6, d^1/Re^{6+}-Ba_2MnReO_6, d^2/Re^{5+}-Pb_2CrReO_6, d^3/Ir^{6+}-Sr_2CaIrO_6, d^4/Ir^{5+}-Sr_2ScIrO_6 and d^5/Ir^{4+}-La_2CuIrO_6 standards, indicating Ta^{5+} in $Ca_{1.8}Mn_{0.2}MnTaO_6$.

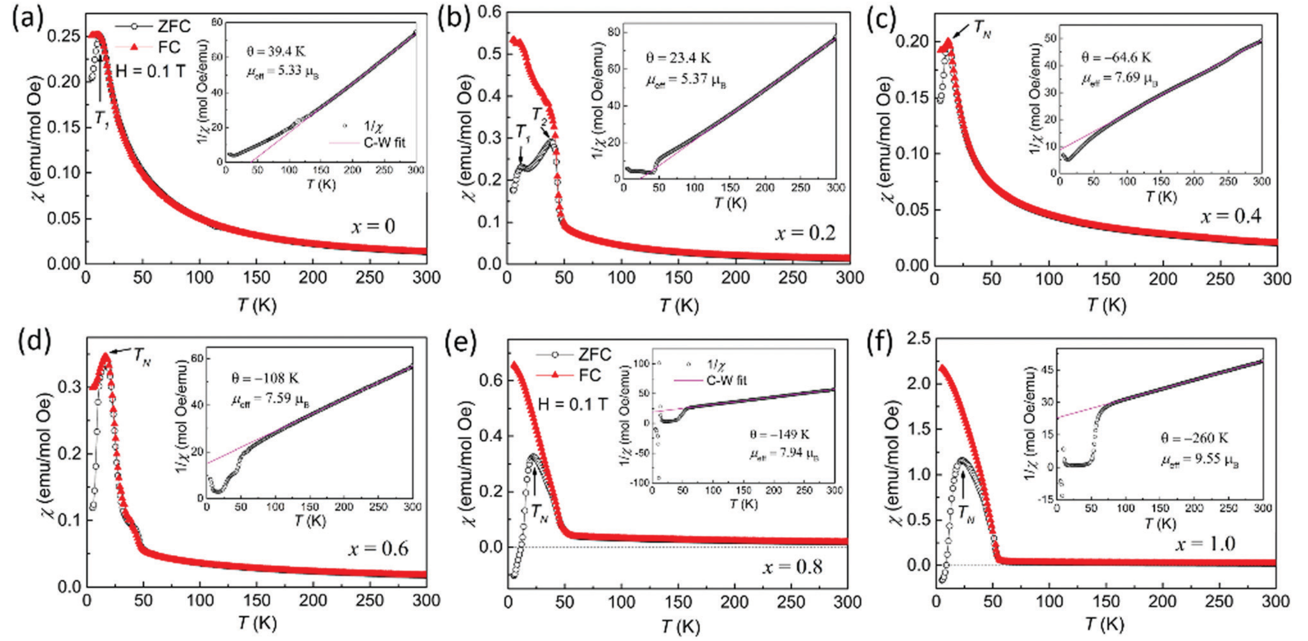

Fig. 7 Magnetic properties of $Ca_{2-x}Mn_xMnTaO_6$. Temperature dependence of the magnetic susceptibilities measured at 0.1 T under zero-field-cooled (ZFC, empty circles) and field-cooled (FC, filled triangles) conditions between 5 and 300 K. (a) $x = 0$; (b) $x = 0.2$; (c) $x = 0.4$; (d) $x = 0.6$; (e) $x = 0.8$; (f) $x = 1$. The insets show the ZFC χ^{-1} *vs.* T curves at 0.1 T with the Curie–Weiss fits.

transition appears at around 114 K, due to a measurement problem with the instrument. As shown in Fig. 7b, two magnetic transitions are clearly exhibited for $x = 0.2$: the temperature at $T_1 = 19.6$ K is nearly identical to $x = 0$, and it is the result of the spin magnetization of Mn^{3+} at the B site. On account of the doping of Mn^{2+} at the A site, an FM transition appeared at $T_2 = 44$ K. The effective magnetic moment ($\mu_{eff} = 5.37\ \mu_B$) could be obtained by CW law fitting, which is close to the theoretical value (5.57 μ_B) corresponding to spin-only A site Mn^{2+} (high-spin d^5) and B site Mn^{3+} (high-spin d^4) moments, as evidenced from the crystal structure and XANES results. With an increase in the dopant, the samples of the $x = 0.4$, 0.6, 0.8 and 1.0 phases display an antiferromagnetic (AFM) state, as shown in Fig. 7c–f. A significant peak in the ZFC curve suggests the onset of an antiferromagnetic transition at T_N. It is noteworthy that the magnitudes of their negative Weiss temperatures are much higher than T_N, suggesting significant magnetic frustration/interaction. The substitution of Ca^{2+} ions by Mn^{2+} can be defined as the ‘‘chemical pressure’’, which can be attributed to the decrease in the magnetic transition temperature.[79,80] Their effective magnetic moments are greater than the calculated values due to magnetic interactions between Mn^{2+} and Mn^{3+}. As exhibited in Fig. 7e and f, another interesting finding is that a negative ZFC $\chi(T)$ is observed for the $x = 0.8$ and 1.0 samples. It has been proposed in the literature that misplaced B-site cations can result in an antiphase boundary coming into being, which is accompanied by short-range FM coupling between Mn^{2+} and Mn^{4+} ions at the B sites, as evidenced by the XPS results, and AFM coupling occurs at the antiphase boundary. In the ZFC mode, a magnetic field of 0.1 T is insufficient to align all frozen clusters and domain spins with the direction of field. In this sense, as the temperature decreases, the spin anti-parallel or tilt state is stabilized, resulting in the residual magnetization tending to be negative. A similar phenomenon occurred in R_2NiMnO_6 (R = Pr, Nd, Y, and Ho) and $La_{2-x}Bi_xCoMnO_6$ ($x = 0$ and 0.1).[81,82]

The isothermal magnetization $M(H)$ was measured at different temperatures from 5 to 300 K under magnetic field between −5 and 5 T. The $M(H)$ results presented in Fig. 8 support this conclusion, with the magnetic hysteresis loop below $T = 10$ K most dramatically evidencing a first-order increasing-field-induced transition out of the AFM state. Samples of $x = 0$ and 0.4 show S-type shaped curves at 10 K, which indicate typical weak canted ferromagnetism, as displayed in Fig. 8a and c, respectively. As shown in Fig. 8b, a hysteresis loop is present in $x = 0.2$ down to the temperature measured ($T = 35$ K), which confirms the presence of FM ordering below the FM transition at $T_C = 44$ K, present even at low temperatures. The other AFM samples also showed a clear hysteresis loop at 10 K, as shown in Fig. 8d and f. Their FM properties are due to an increase in the concentration of induced magnetic moments on Mn at the A site. The magnetic parameters of the CW law fitting of $Ca_{2-x}Mn_xMnTaO_6$ system with $0 \leq x \leq 1.0$ are summarized in Table S5 (ESI†), and have been used to map the magnetic phase diagram shown in Fig. 9. Samples of $x = 0$ and 0.2 were FM dominant phases with T_C = 19.6 and 44 K, respectively. For $Ca_{2-x}Mn_xMnTaO_6$ with $0.4 \leq x \leq 1.0$, it was found that Mn^{2+} at the A site is involved in long-range magnetic ordering, enhancing the AFM order Mn–O–Mn super-exchange with an increase in x, with T_N gradually becoming larger and tends to be constant.

Unlike the other exotic perovskite with 50% of the A-sites occupied by transition metal cations, such as the A-site columnar-ordered $P4_2/n$-type quadruple perovskites $CaMnBReO_6$

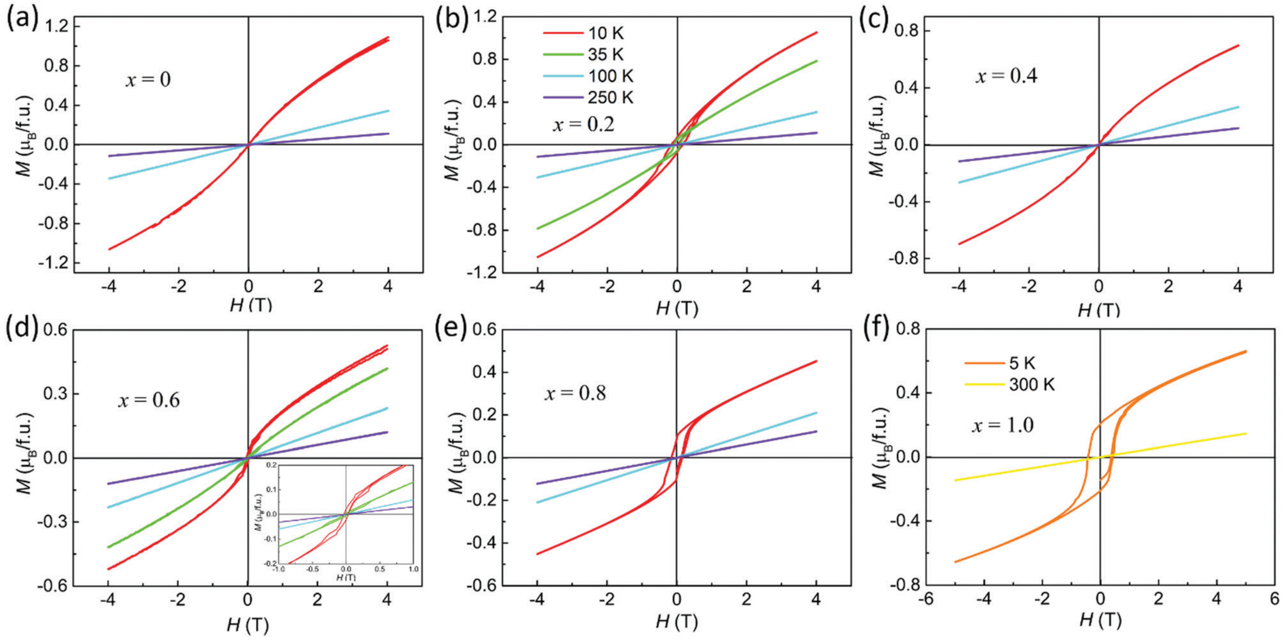

Fig. 8 Isothermal magnetization curves of $Ca_{2-x}Mn_xMnTaO_6$ at 10, 35, 100, and 250 K between −4 and 4 T. (a) $x = 0$; (b) $x = 0.2$; (c) $x = 0.4$; (d) $x = 0.6$; (e) $x = 0.8$; (f) $x = 1$. The inset in (d) shows the expanded region between −1.0 and 1.0 T, showing clear hysteresis loops at different temperatures.

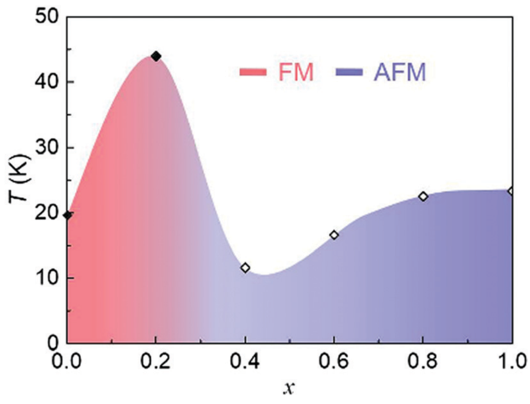

Fig. 9 Schematic magnetic phase diagram of $Ca_{2-x}Mn_xMnTaO_6$. The symbols are the transition temperatures of $Ca_{2-x}Mn_xMnTaO_6$ (filled diamonds for T_C $0 \leq x \leq 0.2$, open diamonds for T_N of $0.4 \leq x \leq 1.0$). The pink area is the ferromagnetic (FM) phase, the blue area for the antiferromagnetic (AFM) phase.

(B = Mn,[20] Fe,[20] Co,[21] Ni[21]), $CaMn_{0.5}Cu_{0.5}FeReO_6$,[20] and $RMnMnSbO_6$ (R = La, Pr, Nd, Sm),[22] and $P4_2mc$ structured $Ca_{1.4}Mn_{0.6}Ti_2O_6$ in $Ca_{2-x}Mn_xTi_2O_6$ ($x \leq 0.6$),[19] either A- or B-site cationic ordering is absent in $Ca_{2-x}Mn_xMnTaO_6$, and the structural formula can be written as $(Ca_{1-x/2}Mn_{x/2})(Mn_{0.5}Ta_{0.5})O_3$, namely $(Ca_{0.5}{}^{2+}Mn_{0.5}{}^{2+})(Mn_{0.5}{}^{3+}Ta_{0.5}{}^{5+})O_3$, other than $CaMnMnTaO_6$ for $x = 1.0$, which is, to the best of our knowledge, for the first time observed in an exotic perovskite with half of the A-sites occupied by small transition metal ions. In $Ca_{2-x}Mn_xTi_2O_6$ prepared under chemical and soft physical pressure, similar A-site Ca/Mn disordering was observed for x below 0.4. However, an A-site columnar-ordered quadruple perovskite, $A_2A'A''B_4O_{12}$, was obtained for $Ca_{2-x}Mn_xTi_2O_6$ with $0.4 \leq x \leq 0.6$.[19] When Ti^{4+} was replaced by Mn/Ta in $Ca_{2-x}Mn_xTi_2O_6$, the A-site columnar-ordering vanished. Probably, the coexistence of B-site Mn^{3+} (Jahn–Teller distortion ion) and B′-site Ta^{5+} (second-order Jahn–Teller distortion ion) does not favour the formation of the A-site columnar ordered perovskite structure $(Ca)_2{}^{A}(Mn)^{A'}(Mn)^{A''}(Mn)_2{}^{B}(Ta)_2{}^{B'}O_{12}$ ($x = 1.0$ case), and the cationic disordering at both the A- and B-sites, together with charge disproportionation of Mn^{3+} into Mn^{2+} and Mn^{4+} at the B-sites, synergically renders a lower energy ground state of the *Pbnm* structure in $Ca_{2-x}Mn_xMnTaO_6$.

Conclusions

In conclusion, we have prepared new exotic perovskite oxides, $Ca_{2-x}Mn_xMnTaO_6$ ($0 \leq x \leq 1.0$), by means of combining chemical and physical pressure techniques. The lower-Mn compounds ($x \leq 0.2$) can be solely stabilized by chemical pressure, while the target phase dominated samples can be achieved at an intermediate physical pressure of 7 GPa for $0.4 \leq x \leq 1.0$. The crystal structure remains *Pbnm* as in Ca_2MnTaO_6, and can be written as $(Ca_{1-x/2}Mn_{x/2})(Mn_{1/2}Ta_{1/2})O_3$ without expected A-site columnar-ordering. Both the XANES and XPS data suggest the formulas $Ca_{2-x}Mn_x{}^{2+}Mn^{3+}Ta^{5+}O_6$ ($0 \leq x \leq 0.6$) and $Ca_{2-x}Mn_x{}^{2+}(Mn^{3+,2+/4+})Ta^{5+}O_6$ ($0.8 \leq x \leq 1.0$). The spin-only A site Mn^{2+} (high spin d^5) and B site Mn^{3+} (high spin d^4) moments enhance ferromagnetic ($x \leq 0.2$) to antiferromagnetic ($0.4 \leq x \leq 1.0$) transition around the boundary of $x = 0.2$. The partial charge disproportionation of the B-site Mn^{3+} into Mn^{2+} and Mn^{4+} $x = 0.8$ and 1.0 introduces negative ZFC magnetization, stemming from the formation of spin antiparallel or ferromagnetic clusters and domains separated by antiphase boundaries. This charge disproportionation over the B-sites makes a synergic contribution towards stabilizing the highly disordered *Pbnm* structure in $Ca_{2-x}Mn_xMnTaO_6$. The present findings update the fundamental understanding of fixing of high-pressure phase within an ambient-pressure phase matrix, and imply that the coexistence of Jahn–Teller distorted ions at the B- and B′-sites should be avoided in $A_2A'A''B_2B_2'O_{12}$ to ensure cationic ordering and strong magnetic interactions.

Conflicts of interest

There are no conflicts to declare.

Acknowledgements

This work was financially supported by the National Science Foundation of China (NSFC-21801253, 11804404 and 21875287) and the National Science Foundation (NSF) Grant No. DMR-1809931. Structural analysis of exotic materials in this study was partly supported by the Research Grant No. 075-15-2019-1886 from the Government of the Russian Federation. The XANES work at the Brookhaven National Laboratory, NSLS-II, was supported by the DOEBES (DE-SC0012704). The NSLS-II work was performed on beamline 7-BM and the authors gratefully acknowledge the invaluable help of the beamline scientists Steven Ehrlich and Syed Khalid.

Notes and references

1 M. A. Peña and J. L. G. Fierro, *Chem. Rev.*, 2001, **101**, 1981–2018.
2 B. Raveau, *Prog. Solid State Chem.*, 2007, **35**, 171–173.
3 S. Vasala and M. Karppinen, *Prog. Solid State Chem.*, 2015, **43**, 1–36.
4 D. Serrate, J. M. D. Teresa and M. R. Ibarra, *J. Phys.: Condens. Matter*, 2007, **19**, 023201.
5 V. M. Goldschmidt, *Die Naturwissenschaften*, 1926, **14**, 477–485.
6 W. Li, E. Ionescu, R. Riedel and A. Gurlo, *J. Mater. Chem. A*, 2013, **1**, 12239–12245.
7 D. Beqiri, V. Cascos, J. Roberts-Watts, E. R. Clark, E. Bousquet, N. C. Bristowe and E. E. McCabe, *Chem. Commun.*, 2019, **55**, 2609–2612.
8 C. J. Bartel, C. Sutton, B. R. Goldsmith, R. Ouyang, C. B. Musgrave, L. M. Ghiringhelli and M. Scheffler, *Sci. Adv.*, 2019, **5**, eaav0693.
9 M. R. Filip and F. Giustino, *Proc. Natl. Acad. Sci. U. S. A.*, 2018, **115**, 5397.
10 H. Zhang, N. Li, K. Li and D. Xue, *Acta Crystallogr., Sect. B: Struct. Sci.*, 2007, **63**, 812–818.
11 P. W. Barnes, M. W. Lufaso and P. M. Woodward, *Acta Crystallogr., Sect. B: Struct. Sci.*, 2006, **62**, 384–396.
12 M. W. Lufaso and P. M. Woodward, *Acta Crystallogr., Sect. B: Struct. Sci.*, 2004, **60**, 10–20.
13 M.-R. Li, P. W. Stephens, M. Croft, Z. Deng, W. Li, C. Jin, M. Retuerto, J. P. Hodges, C. E. Frank, M. Wu, D. Walker and M. Greenblatt, *Chem. Mater.*, 2018, **30**, 4508–4514.
14 M.-R. Li, J. P. Hodges, M. Retuerto, Z. Deng, P. W. Stephens, M. C. Croft, X. Deng, G. Kotliar, J. Sánchez-Benítez, D. Walker and M. Greenblatt, *Chem. Mater.*, 2016, **28**, 3148–3158.
15 M.-R. Li, M. Retuerto, Z. Deng, P. W. Stephens, M. Croft, Q. Huang, H. Wu, X. Deng, G. Kotliar, J. Sánchez-Benítez, J. Hadermann, D. Walker and M. Greenblatt, *Angew. Chem., Int. Ed.*, 2015, **54**, 12069–12073.
16 A. Hossain, P. Bandyopadhyay and S. Roy, *J. Alloys Compd.*, 2018, **740**, 414–427.
17 K. Leinenweber and J. Parise, *J. Solid State Chem.*, 1995, **114**, 277–281.
18 A. Aimi, D. Mori, K.-I. Hiraki, T. Takahashi, Y. J. Shan, Y. Shirako, J. Zhou and Y. Inaguma, *Chem. Mater.*, 2014, **26**, 2601–2608.
19 Z. Li, Y. Cho, X. Li, X. Li, A. Aimi, Y. Inaguma, J. A. Alonso, M. T. Fernandez-Diaz, J. Yan, M. C. Downer, G. Henkelman, J. B. Goodenough and J. Zhou, *J. Am. Chem. Soc.*, 2018, **140**, 2214–2220.
20 G. M. McNally, Á. M. Arévalo-López, P. Kearins, F. Orlandi, P. Manuel and J. P. Attfield, *Chem. Mater.*, 2017, **29**, 8870–8874.
21 E. Solana-Madruga, Y. Sun, Á. M. Arévalo-López and J. P. Attfield, *Chem. Commun.*, 2019, **55**, 2605–2608.
22 E. Solana-Madruga, Á. M. Arévalo-López, A. J. Dos Santos-García, E. Urones-Garrote, D. Ávila-Brande, R. Sáez-Puche and J. P. Attfield, *Angew. Chem., Int. Ed.*, 2016, **55**, 9340–9344.
23 A. A. Belik, *Dalton Trans.*, 2018, **47**, 3209–3217.
24 A. A. Belik, L. Zhang, Y. Matsushita, Y. Katsuya, M. Tanaka and K. Yamaura, *J. Solid State Chem.*, 2019, **275**, 43–48.
25 A. A. Belik, D. D. Khalyavin, L. Zhang, Y. Matsushita, Y. Katsuya, M. Tanaka, R. D. Johnson and K. Yamaura, *ChemPhysChem*, 2018, **19**, 2449–2452.
26 L. Zhang, Y. Matsushita, K. Yamaura and A. A. Belik, *Inorg. Chem.*, 2017, **56**, 5210–5218.
27 S. Zhang, T. Saito, M. Mizumaki, W.-T. Chen, T. Tohyama and Y. Shimakawa, *J. Am. Chem. Soc.*, 2012, **135**, 6056–6060.
28 Y. W. Long, N. Hayashi, T. Saito, M. Azuma, S. Muranaka and Y. Shimakawa, *Nature*, 2009, **458**, 60–63.
29 S. V. Ovsyannikov, E. Bykova, A. Pakhomova, D. P. Kozlenko, M. Bykov, S. E. Kichanov, N. V. Morozova, I. V. Korobeinikov, F. Wilhelm, A. Rogalev, A. A. Tsirlin, A. V. Kurnosov, Y. G. Zainulin, N. I. Kadyrova, A. P. Tyutyunnik and L. Dubrovinsky, *Inorg. Chem.*, 2017, **56**, 6251–6263.
30 S. V. Ovsyannikov, Y. G. Zainulin, N. I. Kadyrova, A. P. Tyutyunnik, A. S. Semenova, D. Kasinathan, A. A. Tsirlin, N. Miyajima and A. E. Karkin, *Inorg. Chem.*, 2013, **52**, 11703–11710.
31 K. Shiro, I. Yamada, N. Ikeda, K. Ohgushi, M. Mizumaki, R. Takahashi, N. Nishiyama, T. Inoue and T. Irifune, *Inorg. Chem.*, 2013, **52**, 1604–1609.
32 S. Mehmood, Z. Ali, Z. Hashmi and S. Khan, *Int. J. Mod. Phys. B*, 2019, **33**, 1950212.
33 T. Locherer, R. Dinnebier, R. K. Kremer, M. Greenblatt and M. Jansen, *J. Solid State Chem.*, 2012, **190**, 277–284.
34 F. Mezzadri, M. Calicchio, E. Gilioli, R. Cabassi, F. Bolzoni, G. Calestani and F. Bissoli, *Phys. Rev. B: Condens. Matter Mater. Phys.*, 2009, **79**, 014420.
35 R. Przeniosło, I. Sosnowska, E. Suard, A. Hewat and A. N. Fitch, *Phys. Rev. B: Condens. Matter Mater. Phys.*, 2004, **344**, 358–367.
36 W.-T. Chen, M. Mizumaki, H. Seki, M. S. Senn, T. Saito, D. Kan, J. P. Attfield and Y. Shimakawa, *Nat. Commun.*, 2014, **5**, 3909.

37 M. S. Senn, W.-t. Chen, T. Saito, S. García-Martín, J. P. Attfield and Y. Shimakawa, *Chem. Mater.*, 2014, **26**, 4832–4837.

38 X. Wang, M. Liu, X. Shen, Z. Liu, Z. Hu, K. Chen, P. Ohresser, L. Nataf, F. Baudelet, H.-J. Lin, C.-T. Chen, Y.-L. Soo, Y.-F. Yang, C. Jin and Y. Long, *Inorg. Chem.*, 2019, **58**, 320–326.

39 A. Prodi, E. Gilioli, R. Cabassi, F. Bolzoni, F. Licci, Q. Huang, J. W. Lynn, M. Affronte, A. Gauzzi and M. Marezio, *Phys. Rev. B: Condens. Matter Mater. Phys.*, 2009, **79**, 085105.

40 F. Mezzadri, G. Calestani, M. Calicchio, E. Gilioli, F. Bolzoni, R. Cabassi, M. Marezio and A. Migliori, *Phys. Rev. B: Condens. Matter Mater. Phys.*, 2009, **79**, 100106.

41 A. A. Belik, Y. Matsushita, Y. Kumagai, Y. Katsuya, M. Tanaka, S. Y. Stefanovich, B. I. Lazoryak, F. Oba and K. Yamaura, *Inorg. Chem.*, 2017, **56**, 12272–12281.

42 T. Kawamoto, K. Fujita, I. Yamada, T. Matoba, S. J. Kim, P. Gao, X. Pan, S. D. Findlay, C. Tassel, H. Kageyama, A. J. Studer, J. Hester, T. Irifune, H. Akamatsu and K. Tanaka, *J. Am. Chem. Soc.*, 2014, **136**, 15291–15299.

43 L. Liu, H. X. Song, X. Li, D. Zhang, R. Mathieu, S. Ivanov, H. Skogby and P. Lazor, *Appl. Phys. Lett.*, 2019, **114**, 162903.

44 H.-P. Su, S.-F. Li, Y. Han, M.-X. Wu, C. Gui, Y. Chang, M. Croft, S. Ehrlich, S. Khalid, U. Adem, S. Dong, Y. Sun, F. Huang and M.-R. Li, *J. Mater. Chem. C*, 2019, **7**, 12306–12311.

45 M. Markkula, A. M. Arevalo-Lopez, A. Kusmartseva, J. A. Rodgers, C. Ritter, H. Wu and J. P. Attfield, *Phys. Rev. B: Condens. Matter Mater. Phys.*, 2011, **84**, 094450.

46 A. A. Belik, Y. Matsushita, M. Tanaka and E. Takayama-Muromachi, *Chem. Mater.*, 2012, **24**, 2197–2203.

47 A. B. Alexei and Y. Wei, *J. Phys.: Condens. Matter*, 2014, **26**, 163201.

48 E. Solana-Madruga, A. J. Dos santos-Garcia, A. M. Arevalo-Lopez, D. Avila-Brande, C. Ritter, J. P. Attfield and R. Saez-Puche, *Dalton Trans.*, 2015, **44**, 20441–20448.

49 G. V. Bazuev, A. P. Tyutyunnik, M. V. Kuznetsov and Y. G. Zainulin, *J. Supercond. Novel Magn.*, 2018, **31**, 2907–2914.

50 A. M. Arevalo-Lopez, F. Stegemann and J. P. Attfield, *Chem. Commun.*, 2016, **52**, 5558–5560.

51 A. M. Arévalo-López, G. M. McNally and J. P. Attfield, *Angew. Chem., Int. Ed.*, 2015, **54**, 12074–12077.

52 C. E. Frank, E. E. McCabe, F. Orlandi, P. Manuel, X. Tan, Z. Deng, M. Croft, V. Cascos, T. Emge, H. L. Feng, S. Lapidus, C. Jin, M. Wu, M. R. Li, S. Ehrlich, S. Khalid, N. Quackenbush, S. Yu, D. Walker and M. Greenblatt, *Chem. Commun.*, 2019, **55**, 3331–3334.

53 Y. Akizuki, I. Yamada, K. Fujita, K. Taga, T. Kawakami, M. Mizumaki and K. Tanaka, *Angew. Chem., Int. Ed.*, 2015, **54**, 10870–10874.

54 Y. Akizuki, I. Yamada, K. Fujita, N. Nishiyama, T. Irifune, T. Yajima, H. Kageyama and K. Tanaka, *Inorg. Chem.*, 2013, **52**, 11538–11543.

55 S. V. Ovsyannikov, A. M. Abakumov, A. A. Tsirlin, W. Schnelle, R. Egoavil, J. Verbeeck, G. Van Tendeloo, K. V. Glazyrin, M. Hanfland and L. Dubrovinsky, *Angew. Chem., Int. Ed.*, 2013, **52**, 1494–1498.

56 M. Murakami, K. Hirose, K. Kawamura, N. Sata and Y. Ohishi, *Science*, 2004, **304**, 855–858.

57 J. Santillán, S.-H. Shim, G. Shen and V. B. Prakapenka, *Geophys. Res. Lett.*, 2006, **33**, L15307.

58 J. Ruiz-Fuertes, T. Bernert, D. Zimmer, N. Schrodt, M. Koch-Müller, B. Winkler, L. Bayarjargal, C. Popescu, S. MacLeod and K. Glazyrin, *Phys. Rev. B*, 2017, **96**, 094101.

59 G. Gou, N. Charles, J. Shi and J. M. Rondinelli, *Inorg. Chem.*, 2017, **56**, 11854–11861.

60 J. Li, S. Lorger, J. K. Stalick, A. W. Sleight and M. A. Subramanian, *Inorg. Chem.*, 2016, **55**, 9798–9804.

61 R. Shannon, *Acta Crystallogr., Sect. A: Cryst. Phys., Diffr., Theor. Gen. Crystallogr.*, 1976, **32**, 751–767.

62 Bruker AXS, Karlsruhe, Germany, 2008.

63 J. Wang, B. Wylie-van Eerd, T. Sluka, C. Sandu, M. Cantoni, X.-K. Wei, A. Kvasov, L. J. McGilly, P. Gemeiner, B. Dkhil, A. Tagantsev, J. Trodahl and N. Setter, *Nat. Mater.*, 2015, **14**, 985–990.

64 S. Ali, W. Khan, G. Murtaza, M. Yaseen, S. M. Ramay and A. Mahmood, *J. Magn. Magn. Mater.*, 2017, **441**, 113–123.

65 T. K. Mandal, V. V. Poltavets, M. Croft and M. Greenblatt, *J. Solid State Chem.*, 2008, **181**, 2325–2331.

66 P. W. Barnes, M. W. Lufaso and P. M. Woodward, *Acta Crystallogr., Sect. B: Struct. Sci.*, 2006, **62**, 384–396.

67 M. P. Seabra, M. Avdeev, V. M. Ferreira, R. C. Pullar and N. M. Alford, *J. Eur. Ceram. Soc.*, 2003, **23**, 2403–2408.

68 A. R. Denton and N. W. Ashcroft, *Phys. Rev. A: At., Mol., Opt. Phys.*, 1991, **43**, 3161–3164.

69 G. Popov, M. Greenblatt and M. Croft, *Phys. Rev. B: Condens. Matter Mater. Phys.*, 2003, **67**, 024406.

70 T. K. Mandal, V. V. Poltavets, M. Croft and M. Greenblatt, *J. Solid State Chem.*, 2008, **181**, 2325–2331.

71 F. Bridges, C. H. Booth, G. H. Kwei, J. J. Neumeier and G. A. Sawatzky, *Phys. Rev. B*, 2000, **61**, R9237.

72 K. Zhong, B. Zhang, S. Luo, W. Wen, H. Li, X. Huang and L. Chen, *J. Power Sources*, 2011, **196**, 6802–6808.

73 M. Retuerto, M.-R. Li, P. W. Stephens, J. Sánchez-Benítez, X. Deng, G. Kotliar, M. C. Croft, A. Ignatov, D. Walker and M. Greenblatt, *Chem. Mater.*, 2015, **27**, 4450–4458.

74 M. A. Laguna-Marco, P. Kayser, J. A. Alonso, M. J. Martínez-Lope, M. van Veenendaal, Y. Choi and D. Haskel, *Phys. Rev. B: Condens. Matter Mater. Phys.*, 2015, **91**, 214433.

75 Z. Huang, W. Zhou, C. Ouyang, J. Wu, F. Zhang, J. Huang, Y. Gao and J. Chu, *Sci. Rep.*, 2015, **5**, 10899.

76 H. R. Barai, A. N. Banerjee and S. W. Joo, *J. Ind. Eng. Chem.*, 2017, **56**, 212–224.

77 M. Yonemura, T. Kohigashi, A. Yamada, N. Sonoyama, H. Kobayashi, T. Kamiyama and R. Kanno, *Electrochemistry*, 2003, **71**, 1160–1161.

78 E. Pollert, *Int. J. Inorg. Mater.*, 2000, **2**, 661–670.

79 A. A. Belik, Y. Matsushita, M. Tanaka and E. Takayama-Muromachi, *Angew. Chem., Int. Ed.*, 2010, **49**, 7723–7727.

80 A. Hauser, N. Amstutz, S. Delahaye, A. Sadki, S. Schenker, R. Sieber and M. Zerara, *Chimia*, 2002, **56**, 685–689.

81 M. Nasir, S. Kumar, N. Patra, D. Bhattacharya, S. N. Jha, D. R. Basaula, S. Bhatt, M. Khan, S.-W. Liu, S. Biring and S. Sen, *ACS Appl. Electron. Mater.*, 2019, **1**, 141–153.

82 Y. Bai, Y. Xia, H. Li, L. Han, Z. Wang, X. Wu, S. Lv, X. Liu and J. Meng, *J. Phys. Chem. C*, 2012, **116**, 16841–16847.